



OPEN Reflective metasurface for 5G & beyond Wireless communications

Monisha Selvaraj^{1,3}, Ramya Vijay^{2,3}✉ & Rajesh Anbazhagan²

This paper presents a scalable reflective metasurface design optimized for 5G and beyond (B5G) wireless communications, featuring a unique combination of passive metasurface elements. The proposed design emphasizes a less complex structural configuration, facilitating easy scalability and cost-effective fabrication. By implementing a single-layer structure, the metasurface enables straightforward integration with existing B5G infrastructure and demonstrates compatibility with emerging intelligent surface technologies, such as Reconfigurable Intelligent Surfaces (RIS). The dual-polarization capabilities of the metasurface ensure angular stability in reflection, enhancing signal reliability and performance in diverse communication environments. Theoretical analyses, supported by experimental validation, showcase the metasurface's effectiveness in addressing the challenges of modern wireless communication systems, paving the way for its practical application in next-generation communication.

Keywords 5G & Beyond, Metasurface, Reflecting Metasurface, Reconfigurable Intelligent Surface

Nowadays, an increasing need for higher data rate, lower latency, and communication in high-speed data transmission/reception in the fifth generation (5G) and beyond 5G driven by the rapid growth of wireless communication. Multiple technologies have been offered in current research years to accomplish these goals, like millimetre wave (mm Wave) communication, Cooperative communication, and massive multiple-input multiple-output (MIMO) emerging as the most popular contenders¹. The technologies mentioned above can improve the bandwidth efficiency of wireless devices significantly. Still, they typically come at a higher cost in terms of hardware, power consumption, and installation cost because they require additional active antennas and added expensive radio frequency (RF) chains that operate at higher frequency bands. Therefore, introducing reflective surface to the wireless system can be a feasible solution to improve signal coverage and development of smart systems remains an ongoing and challenging subject.

Intelligent reflecting surface (IRS) and its many counterparts have newly come to light as a novel and promising approach to the problem as mentioned earlier^{2,3}. IRS is a two-dimensional metasurface with numerous reconfigurable reflecting elements connected to an intelligent controller that can independently control the phase and amplitude according (referred to as a "reflection coefficient") to the incident EM wave at each element in the surface. However, the design and execution of IRS supported wireless systems require a massive array of reflecting elements. The Frequency Selective Surface (FSS) can be a good choice due to the reflect/transmit/absorb characteristics of the EM incident signal. It is widely used in electromagnetic shielding^{4,5}, radomes, stealth technology, and RF (radio frequency) filters to manage signal propagation. Each component of a conventional FSS is periodic and resonates at the resonance frequency. In signal communications, they have frequently been used to offer spectral filtering. Additionally, they are employed in creating antenna radomes, diplexers, and beam splitters⁶. The periodicity of FSSs is typically half that of the resonant frequency's wavelength⁷. Primarily for FSS, multilayer structures are used for high frequency applications⁸⁻¹¹ that complicate the fabrication.

Though FSS is a better choice for this application, a metasurface is a good candidate to address space and fabrication constraints because "meta-atoms" are sub-wavelength, giving them additional benefits over a conventional FSS. For many applications with limited size¹², the sub-wavelength periodicity makes it possible to load a lot of unit cells into a small area. In addition, metasurface can respond steadily to changes in the angle of incidence of the illuminating EM wave due to the small size of the unit cell. Once the metasurface has been fabricated, the response of the metasurface is fixed, and its sensitivity to reflection and transmission cannot be altered¹³. However, since metasurface response is based on localised control, reconfigurable implementation in metasurface is much easier for IRS applications. Thus, EM skins can be effectively utilized for IRS applications.

Hence, in this paper, the proposed design of metasurface could enhance 5G and beyond by passively relaying signals near base stations, functioning as an Intelligent Reflecting Surface (IRS) to optimize signal paths, and

¹Department of ECE, K Ramakrishnan College of Technology, Trichy, Tamil Nadu, India. ²School of EEE, SASTRA University, Thanjavur, Tamil Nadu, India. ³These authors contributed equally: Monisha Selvaraj and Ramya Vijay. ✉email: ramyavijay@ece.sastra.edu

extending coverage for user equipment in weak-signal areas. This proposed structure is highly supportive structure for RIS, due to minimal infrastructure changes.

Literature Survey

With the shift toward beyond-5G networks, nowadays multi-layer surface designs are gaining traction as a transformative technology particularly at high frequencies, such as millimeter-wave and terahertz (THz) bands¹⁴. This section reviews recent developments in multi-layer surface design, materials, and applications in the context of high-frequency communication.

For instance¹⁵, introduced a three-layer surface with varied unit cell geometries, achieving enhanced bandwidth and significant improvements in beam steering. Similarly¹⁶, employed stacked frequency-selective surfaces in a multi-layer configuration, demonstrating optimized signal control for beamforming and interference reduction. These architectures highlight the potential of multi-layer surfaces to support the increased demands of beyond-5G networks. Similarly, the paper⁵ explains multi layered design helps in achieving efficient output for specific application where dimension plays a major role. While designing the multilayer structure, the choice of materials is crucial in determining the performance of multi-layer surfaces, especially at higher frequencies. Metals like copper and silver, and emerging materials such as graphene and liquid crystals, are commonly used due to their conductive and tunable properties. Graphene, in particular, has shown promise in tunable surfaces due to its excellent conductivity at THz frequencies, as demonstrated by¹⁷. By applying a voltage bias, graphene-based surfaces can adjust phase and amplitude dynamically, providing reconfigurability ideal for high-frequency applications¹⁸.

Further, multi-layer surfaces have found several applications in beyond-5G, particularly in beamforming and intelligent reflecting surfaces (IRS), which can enhance signal propagation in dense urban environments. The paper¹⁹ showcased a surface-based IRS that could dynamically redirect signals to avoid obstacles and reduce path loss. Additionally, the ability of multi-layer surfaces to create reconfigurable holograms has been explored by²⁰, allowing spatial modulation and data encoding, thus maximizing bandwidth for high-density networks. Recent advancements include the use of micro-electromechanical systems (MEMS) and liquid crystal layers, which allow for precise and rapid tuning. The author²¹ integrated MEMS switches into a multi-layer surface to control the phase and polarization of reflected waves, achieving rapid adaptation to changing network conditions. Additionally, artificial intelligence (AI) techniques are being investigated to optimize surface configurations in real time, enhancing network efficiency and reducing latency²².

Even though multi-layer surfaces are present promising applications, several challenges persist. They are inter-layer interactions, in which designs can lead to unwanted coupling effects. Multi-layer designs with phase change materials like graphene, liquid crystals face challenges in achieving independent layer responses, which is critical for devices that require precise and tunable control^{23,24}. Such coupling can limit the ability to manipulate light effectively across multiple layers and reduce the achievable bandwidth. Also, these type of surfaces leads to increases the thickness and bulkiness in the designs. Multi-layered structures can add significant thickness, making them unsuitable for applications requiring compact or flexible components, such as in portable or wearable optics.

The paper²⁵ intricate fabrication processes required for multi-layer surfaces, where high-precision alignment and layer-by-layer stacking increase both the cost and potential for error. It highlights that small misalignments between layers can degrade performance and reduce efficiency, making the fabrication of multi-layer surfaces challenging, especially for large areas.

And another one main challenge is the material compatibility issues that arise in multi-layer surfaces, especially when different layers require distinct material properties (e.g., refractive index, thermal expansion). Achieving stability and performance under operational conditions often involves challenging material choices, especially for applications in variable environments or high temperatures^{26–28}.

From the study^{29,30}, it illustrates that the multi-layer surfaces face complexity in design, more space occupation, high fabrication costs and material compatibility issues to performance constraints due to inter-layer interactions. Although multi-layered designs can provide enhanced functionality, these challenges limit their scalability, cost-effectiveness, and integration potential in practical applications, requiring further advancements in materials, fabrication, and design.

In this paper, our research focuses on scalable surface design with the unique combination of passive metasurface elements, with less complexity structure design, easy scalability and cost-effective material for fabrication. Especially, be designing single layer structure, it is easier integration with B5G infrastructure and compatibility with new intelligent surface technologies like Reconfigurable Intelligent Surface (RIS).

Design methodology

An efficient metasurface must have the appropriate EM characteristics and behave steadily under various oblique incidence and polarisation to achieve good reflection. In paper³¹, they classified the conventional structures based on array element. Figure 1 depicts the four primary types of surface element groupings that have been classified generally³¹. The first group comprises centrally connected or N- poles, such dipoles, tri-poles, square-spirals, and Jerusalem crosses; the second group consists of looped forms, like circular, square, hexagonal loops and so on; the third group consists of solid interiors or patch shapes of various shapes; and the fourth group consists of mixtures of above mentioned. The designers choose array elements from any of these groupings and/or utilize a combination of these, according to the possible application.

The inter-element width in group 1 can be significantly decreased to experience an exceptionally broad bandwidth with suitable element design. Choosing a group-2 element with a bigger loop area improves both bandwidth and stability of angle³². For broad-band applications, basic circular loops, square loops, and advanced loop elements have been used. The surface reaches resonance when the loop element's circumference,

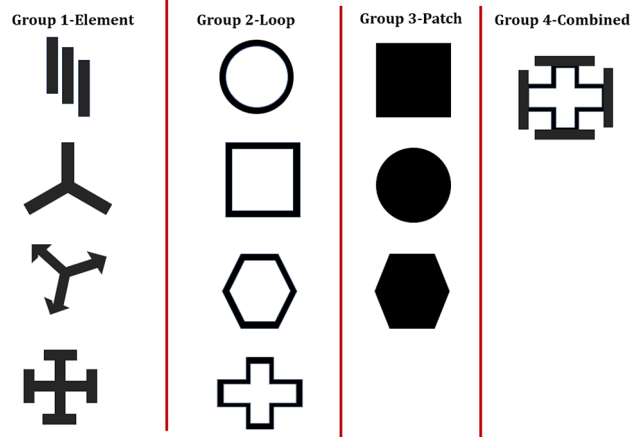


Fig. 1. Various shapes of array elements.

or perimeter, equals a whole wavelength. It is discovered that by altering the form of these loop parts, a wide bandwidth can be obtained. Group 3, which consists of solid internal pieces, is best used as a low-profile structure when combined with comparable elements that are located nearby. Group 4, on the other hand, is made up of combinations of any group to attain several qualities in a single construction. Nowadays, many researchers widely used combinational structures⁵ for various applications like band-stop characteristics and so on.

• Evolution of unit cell

Inspired by group 4 structures, we designed our proposed reflective metasurface design which covers 12–18 GHz of operational band. The choice of 15.48 GHz (Ku band) is strategic for future 5G/B5G as it complements sub-6 GHz and mmWave bands by offering stable medium-distance coverage and high data rates. It supports satellite and backhaul communications, essential for expanding 5G infrastructure, especially in rural areas. This frequency range from 7 GHz to 24 GHz can facilitate extensive coverage areas and substantial capacity, particularly in light of the novel technological developments associated with 6G. For supporting expansive use cases, the X-band and Ku-band spectra are widely examined. Additionally, this frequency may align with future spectrum expansions, thereby rendering the metasurface design adaptable to evolving communication requirements.

Square loop structure

Initially, we started designing the group 2 loop structure because of its angular stability and wider bandwidth behaviors. From the study of paper³³, the geometric design of the square loop in metasurface offers a fascinating platform for manipulating electro-magnetic waves with remarkable precision. By leveraging the unique properties of square loop geometry, engineers and researchers can explore novel techniques to advance the capabilities of 5G and beyond wireless communication systems.

In this paper, we choose metallic structure for achieving reflective characteristics. The metallic structure can be designed to reflect electromagnetic waves at certain frequencies based on its structure geometry and size. Especially loop structure and its dimensions are close to half the wavelength of the target frequency, it will create a strong resonant response, reflecting most of the incident wave energy. Then the results like the reflection coefficient (S11) and transmission coefficient (S21) of the metallic loop structure helps to conclude that structure is reflective or transmissive.

One of the key features of the square loop structure is customizability, which means it has the ability to retain its characteristics even though any structures are combined with it. As a result, the deployment of square loop metasurface can significantly enhance the overall performance of future wireless communication systems.

The overall length of the square loop (d) structure is calculated using the Eqs. (1),

$$d = \frac{C}{4f_{res}} \quad (1)$$

Where, c is the velocity of light, f_{res} is the operating frequency. Here, we construct the square loop length for the center frequency of Ku band as 15 GHz.

Initially, the width of the square loop (w) structure is calculated using the transmission line width Eq. (2).

$$w = \frac{7.48 \times h}{e^{z_0} \frac{\sqrt{r+1.41}}{87}} - 1.25 \times t \quad (2)$$

Where h is the thickness of the substrate, t is the metal thickness, Z_0 is the impedance, r is the value of the permittivity of material used. Formerly according to the perimeter of the loop element the bandwidth can be achieved. So, the parameter analysis has to be done for achieving the operating band of 12–18 GHz shown in

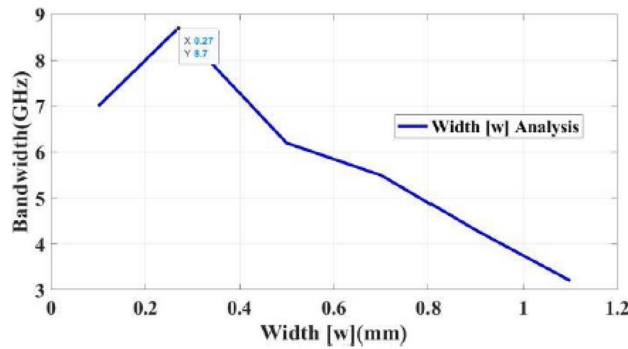


Fig. 2. Parameter analysis for width of the square loop.

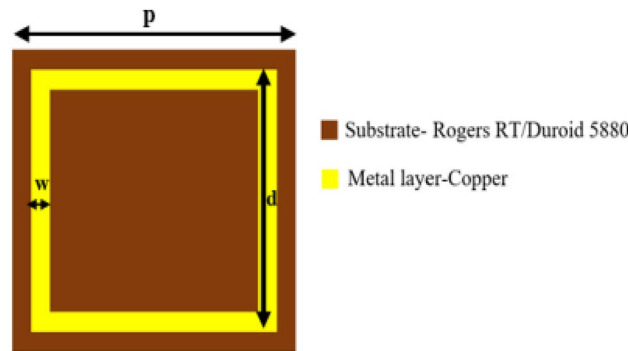


Fig. 3. Geometry of Square loop structure.

Parameters	p	d	w	h	t	Z0	ϵ_r
Values	4.5 mm	4.3 mm	0.27 mm	0.508 mm	0.035 mm	50 ohms	2.2

Table 1. Dimensions of the square loop structure.

Fig. 2. From the formula, the value of w is calculated as 1.1. Figure 2 depicts at 0.27 mm of value the structure covers the wider bandwidth of 8.7 GHz.

In this structure, copper (Cu) is the preferred metal layer due to its high conductivity and low cost. The middle layer acts as a substrate that controls the propagation of the electromagnetic (EM) wave. It separates the top and bottom layers, and the substrate selection is crucial for the metasurface’s proper functioning. The relative permittivity (ϵ_r) and thickness (t) are the parameters that affect the frequency response of the sub- strates. For high-frequency applications, materials with lower relative permittivity are preferred. Rogers RT/Duroid 5880, with an ϵ_r value of 2.2, is the substrate selected for this device. The square loop structure is optimized and designed with the overall unit cell dimension of $4.5 \times 4.5 \times 0.508 \text{ mm}^2$ shown in Fig. 3. and values of the parameters used for the design are tabulated in Table 1.

A viable substitute for full wave computations in surface investigation is the Equivalent Circuit model (ECM), which provides a quick and easy method. This model, which builds the surface from equivalent lumped inductive (L) and capacitive (C) components, is supported by the transmission line connection. Marcuvitz created a quasi-static ECM for conducting strips, which makes it possible to calculate the values for L and C. The ECM for the square loop structure is displayed in Fig. 4 (b). The horizontal gratings function as a C impedance and the vertical strips as a L impedance in the ECM for transverse electrical (TE) wave incidence.

The L and C values of the ECM are often computed using (3) and (4), where θ is the incidence angle with respect to the normal incidence and d , p , w , and g (space between one element to another) are the square loop’s dimensions in Fig. 4 (a).

$$\frac{\omega_r L_1}{Z_0} = \frac{p}{d} \cos \frac{p}{\lambda} \ln \left[\csc \frac{\pi \omega}{2p} \right] \tag{3}$$

$$\frac{\omega_r C_1}{Z_0} = 4 \frac{p}{d} \sec \frac{p}{\lambda} \ln \left[\csc \frac{\pi g}{2p} \right] \times 0.5 (\epsilon_r + 1) \tag{4}$$

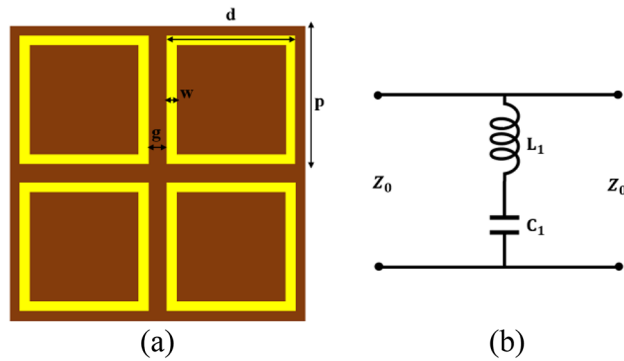


Fig. 4. ECM of Square loop structure.

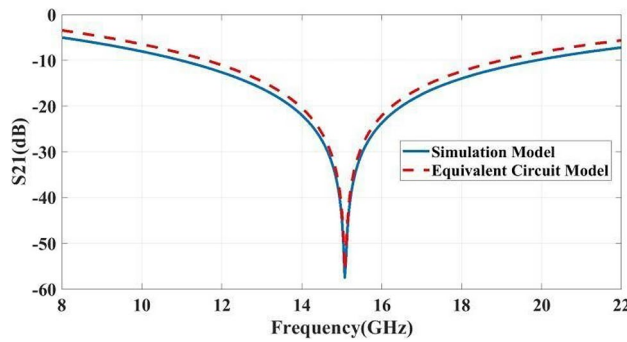


Fig. 5. Comparison results of Square loop structure.

In this work, the model has been designed using an EM simulation tool CST Studio Suite and the ECM has been designed using the Keysight’s Advanced Design System (ADS). Figure 5 shows good agreement with the square loop structure and equivalent circuit model, and it resonates at the operating band of 10.9–19.8 GHz which covers Ku band of frequency.

With the uncertainty in the direction of the EM wave, the operating frequency of the surface structure may affect and deviate the frequency. That should be a major problem while designing the surface for applications that require adaptability to dynamic environments. Thus, the proper selection of the surface structure is essential, and that structure must be consistent at various incident angles.

The square loop structure has undergone an angular stability analysis for various incident angles at both the modes of operations (Transverse Electric (TE) and Transverse Magnetic (TM)). Figure 6 shows that up to 85° of incident electromagnetic waves are roughly or close to the operating frequency. However, there is still a maximum frequency variation of around 0.5 GHz in TE mode and approximately 1.5 GHz in TM mode. In order to increase the angular stability, we are moving towards the next configuration.

Combined loop structure

The second arrangement adds additional loop structure to the intended square loop structure since loop structures exhibit higher angular stability features. From the survey paper³², the number of sides in a polygon can influence the bandwidth over which the surface can operate. Octagons have a larger number of sides compared to other loop structures in group 2, potentially allowing for broader frequency coverage as well as angular stability.

There exist two distinct approaches for designing an integration of the two loop structures are shown in Fig. 7. Type 1 consists of two separate loop structures which results multiband structure and Type 2 consists of merged loop structures which results in wideband structure shown in Fig. 8.

From above graph (Fig. 8), the type 2 structure is more efficient structure for our case. Then we validate this type 2 combined loop structure model, using the ECM model analysis. Then while integrating of the octagonal loop with a conventional square loop. The conventional octagonal loop²¹ ECM can be calculated using (5),

$$L_2 = 2 \times 10^{-13} \times l \times \left(\ln \frac{2L}{w_1 + t} \right) + 0.77 + \left(\frac{w_1 + t}{l} \right) \tag{5}$$

$$C_2 = \frac{r w_1 l}{t} \tag{6}$$

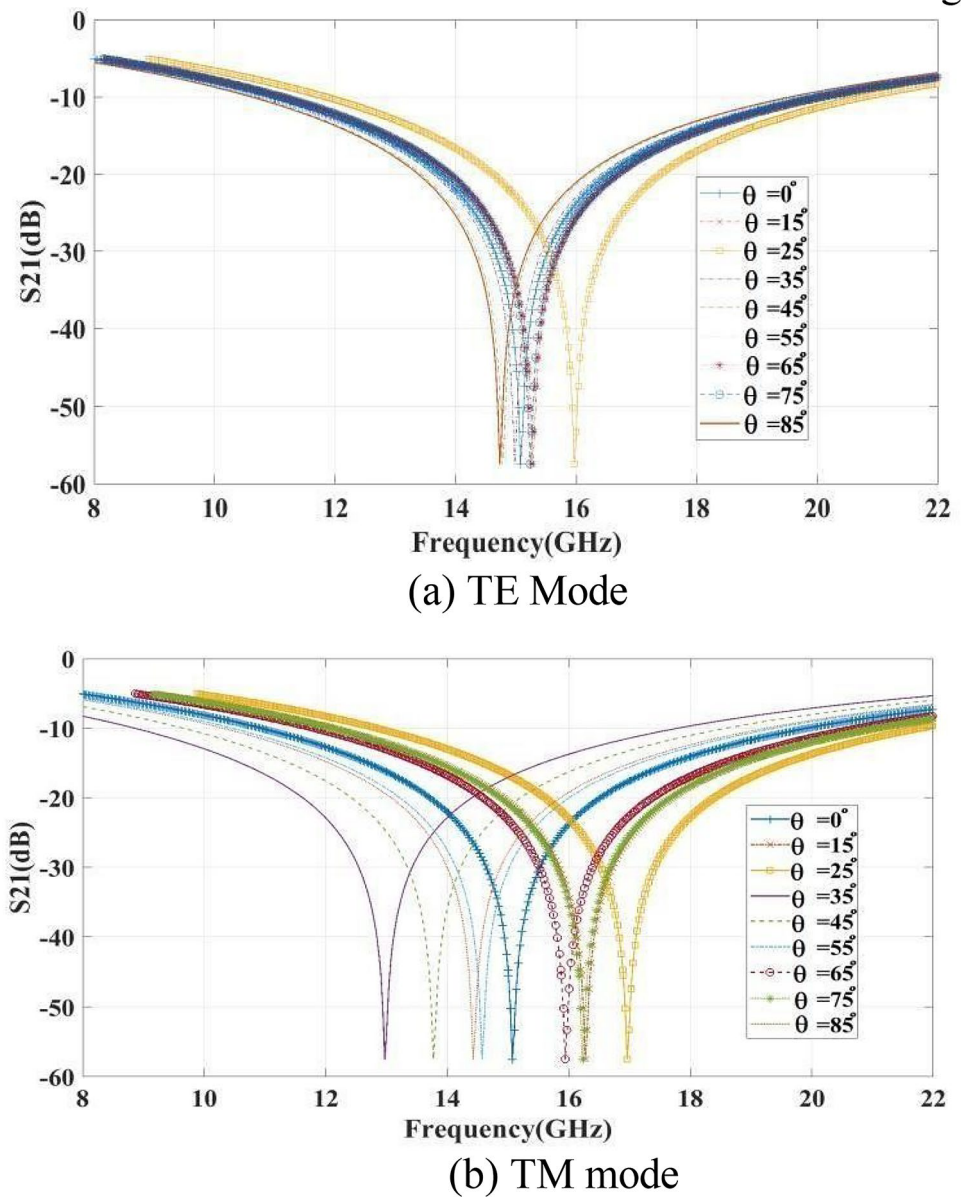


Fig. 6. Angular stability analysis of square loop structure.

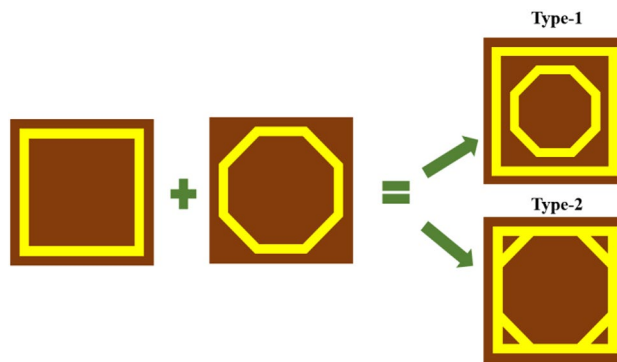


Fig. 7. Types of combining loop structure.

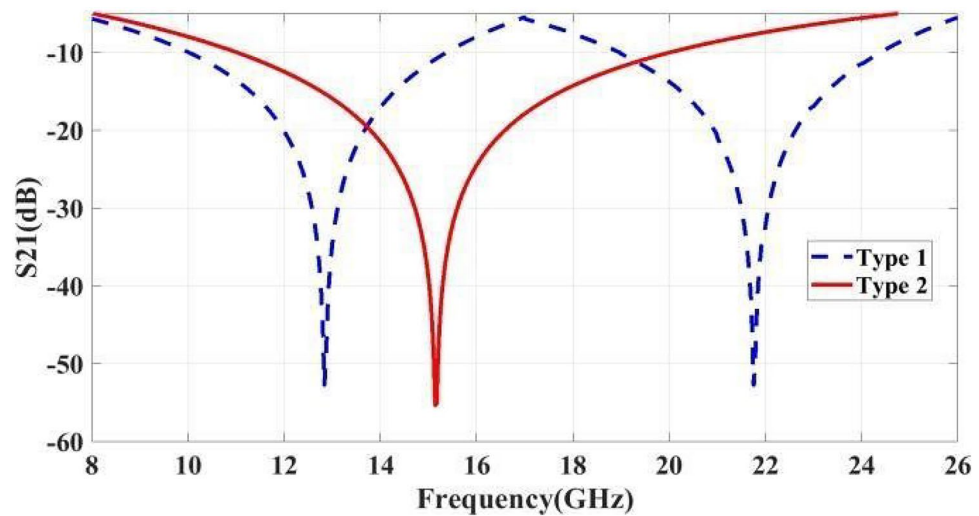


Fig. 8. Result comparisons of different combinations of loop structures.

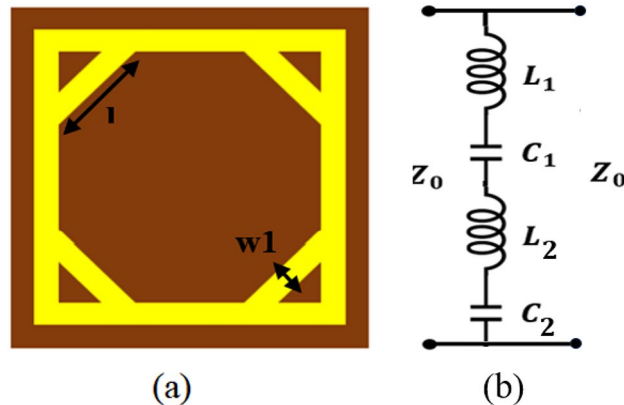


Fig. 9. ECM for combinations of loop structures.

Where l and w_1 are the length and width of the octagonal loop structure. $L_2 = 0.0012$ nH is calculated using (5). The capacitor C_2 is added at four corners of the structure by combining the two-loop structure. That can be calculated using the perimeter of the triangular value using (6), $C_2 = 0.0028$ pF.

Figures 9 and 10 shows good agreement with the combined loop structure and equivalent circuit model, and it resonates at the operating band of 11–20.3 GHz which covers Ku band of frequency.

The transmission properties of the combined loop structure for TE and TM polarized EM fields at different angles of incidences up to 85° are depicted in Fig. 11. At its operating frequency of 15 GHz, the proposed combined loop structure delivers a steady response with slight variation for every angle of EM wave incidence with frequency shift of 0.1 GHz at TE mode and 0.29 GHz at TM Mode. As a result, compared with the square loop structure, the combined structure complies with better angularly stability criteria.

In order to increase the angular stability and steering reflected EM wave towards the intended receiver. We are moving towards the next configuration.

Three legged loaded with combined loop structure

The Fig. 12, third arrangement adds additional element structure to the intended combined loop structure since element structures exhibit broader bandwidth, higher angular stability, and EM Phase control features. From the survey paper³¹, the three-legged element adjusts the phases and shapes of the EM waves, precisely steering them towards the intended receiver, even in the presence of obstacles or interferences. Three-legged element contains the leg with 120° rotation, which helps for tuning flexibility of EM waves.

Then we validate this type 3 combined loop structure with three-legged model, by using ECM model analysis. By considering type 3 structure, the current distribution plot helps to construct the LC circuit. The current distribution plot and its appropriate ECM is optimized and shown in Fig. 13. In that the L_3 and C_3 values of the type 3 structure is tuned and combined with the type 2 ECM model. Then the tripole structure introduced

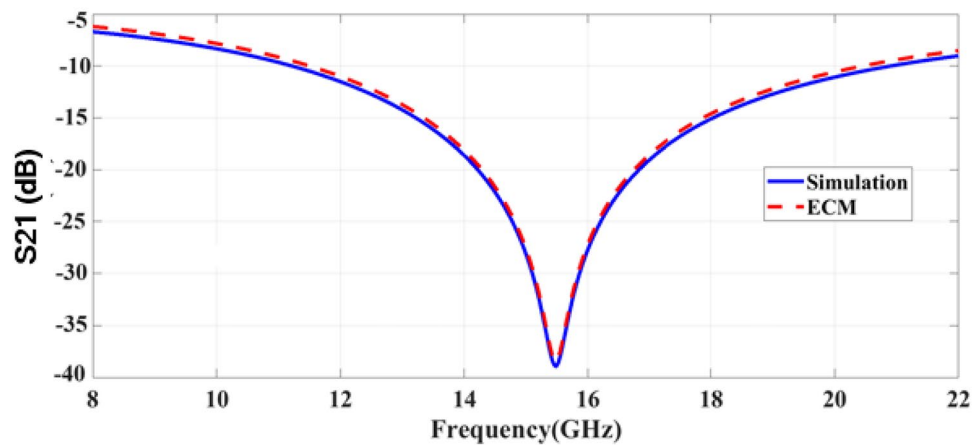
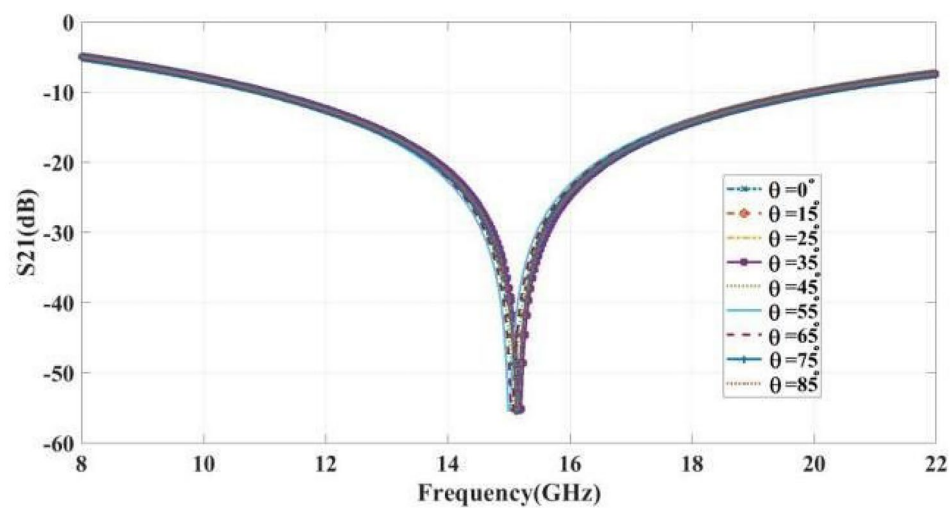
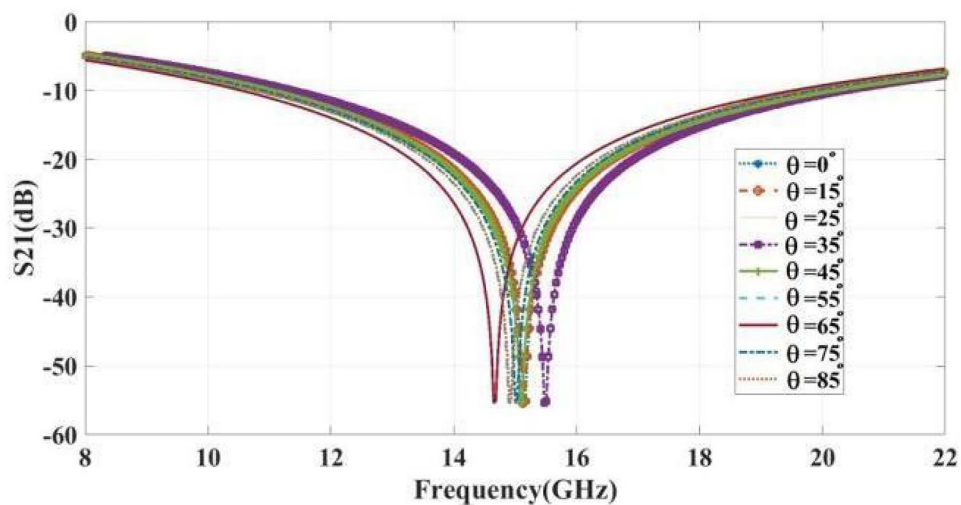


Fig. 10. Comparison results of combined loop structure.



(a) TE Mode



(b) TM Mode

Fig. 11. Angular stability analysis of combined loop structure.

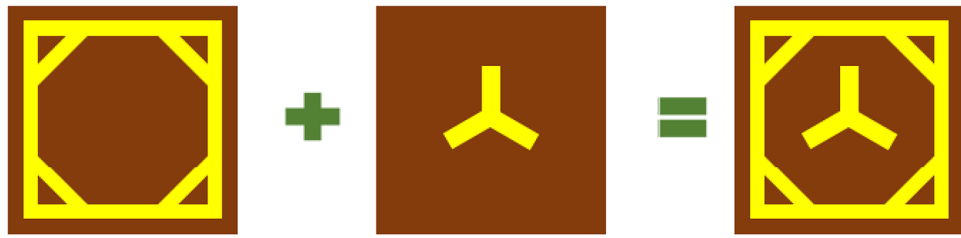


Fig. 12. Combining loop structures with three-legged element.

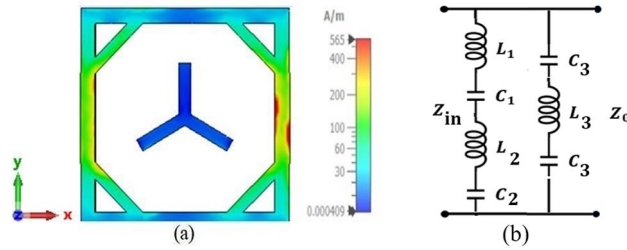


Fig. 13. ECM for combined loops with three-legged structure.

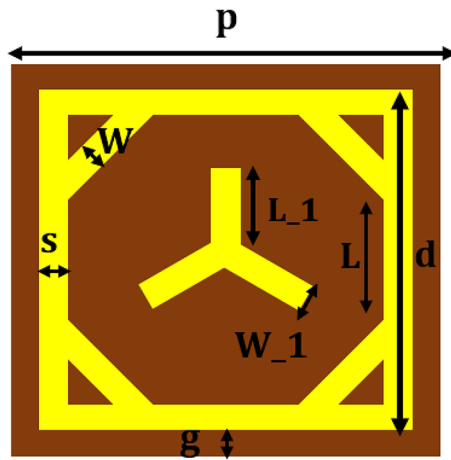


Fig. 14. Geometry of combined loops with three-legged structure.

Parameters	p	d	S	G	L	L_1	W_1	h
Values (mm)	4.5	4.2	0.3	0.2	1.4	1.05	0.25	0.508
Components	L_1	L_2	L_3	C_1	C_2	C_3		
Values	0.7 nH	4 nH	1.9 nH	0.25 pF	1 pF	28 pF		

Table 2. Dimensions of proposed structure.

the series of inductor and capacitor with parallel octagonal loop structure. The value of the capacitor C_3 can be calculated using the formula (7) $C_3 = 0.0028$ pF, and the inductor value is optimized as $L_3 = 0.009$ nH.

$$C_3 = \frac{\epsilon_0 \epsilon_r W_1 L_1}{t} \quad (7)$$

The final geometry of the unit cell has been shown in Fig. 14 and values of its ECM model and its values are tabulated and Table 2.

Figure 15 evidence that the proposed three leg structure resonates at the operational band of 11–19.9 GHz, which covers the Ku band of frequency which is same as that of the type 2 structure and exhibits strong agreement with the combined loop with three-legged element and equivalent circuit model.

Figure 16 shows the various incident angle (0° to 85°) curves in the type 3 proposed structure's TE and TM modes. For each incident signal (0° to 85°) from the source, the proposed type 3 structure reflects the signal in the same frequency with very minute frequency shifting of 0.02 GHz at TE mode and 0.19 GHz at TM mode. The Ku band is covered by type 3, in spite of its frequency shifting.

Based on the above analysis, it is evident that the proposed structure employ square loop metasurface because of their high level of customize ability to adjust the geometry of the loops to meet our specific design requirements. Further, it is integrated with an octagonal loop metasurface to reduce coupling between neighbouring elements and significantly enhance the metasurface's overall performance. This integrated loop structure ensured that the electromagnetic waves reflected from the source were polarized in a specific direction, considerably reducing signal degradation, and improving overall quality. The using a tripole metasurface with diodes in the integrated loop helps to adjust the phases of the waves, precisely steering them towards the intended receiver, even in the presence of obstacles or interference.

Angle Mean deviation

The Angular stability analysis studies how surfaces function when subjected to different angles of incidence or viewing. This analysis is crucial in determining the effectiveness of surfaces in manipulating electromagnetic waves. It ensures the consistent and reliable performance of surfaces regardless of the angle at which they are viewed or interacted. The proper selection of the structure helps to reduce variations in resonance frequency. Therefore, angle mean deviation (AMD)¹⁸ can be used to calculate the frequency deviation, and it can determine the angular stability for TE and TM modes of operation under varying incidence angles using (7).

$$f_{as} = \sum_{i=0}^n \frac{f_r^{normal} - f_r^{ai}}{n f_r^{normal}} \times 100\% \quad (7)$$

Where f_{as} , f_r^{normal} , f_r^{ai} , and n are the deviation in the resonant frequency, the resonating frequency at various incidence angles, and the number of incidence angles, respectively.

By defining the derivative of the reflected signal concerning the incident angle, the angle mean deviation (AMD) quantifies angular stability, which is shown in under the heading 2.2 angle mean deviation. Using Eq. 7 and data from the Figs. 6, 11 and 16, we have calculated the angular stability. The calculated value is presented in Supplementary Table S1 and the comparison graph is plotted and shown in Fig. 17.

$$n = 9$$

$$f_r^{normal} = 15.48 \text{ GHz}$$

Figure 17 shows the various configurations of the suggested structure with its Angle Mean Deviations (AMD) of both the modes of operations. With this collected data, we can identify the frequency deviation. The calculated angle mean deviation (AMD) depicts the minimum percentage of frequency deviation 1.89–0.45% for TE mode and from 3.84 to 2.46% for TM mode. According to Fig. 3 chart, Configuration 3 has improved angular stability.

Polarization analysis

One crucial aspect of surface design is polarization insensitivity. This means that the polarization of the incoming wave does not affect the device's performance. Polarization sensitivity is a common issue with traditional devices that can reduce efficiency and performance in real-world scenarios where the polarization of the wave is unknown or uncontrolled. Polarization insensitivity enables the design of devices and systems that

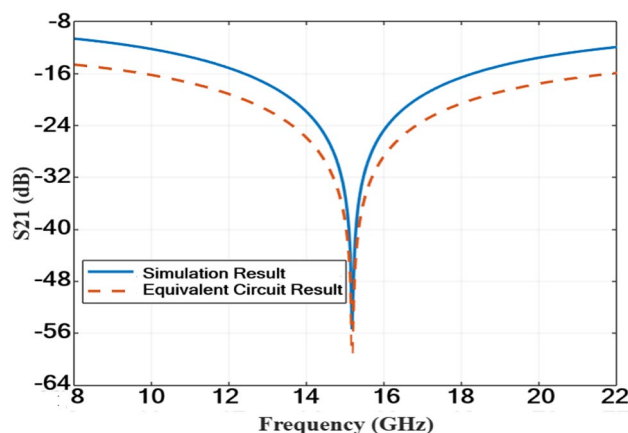
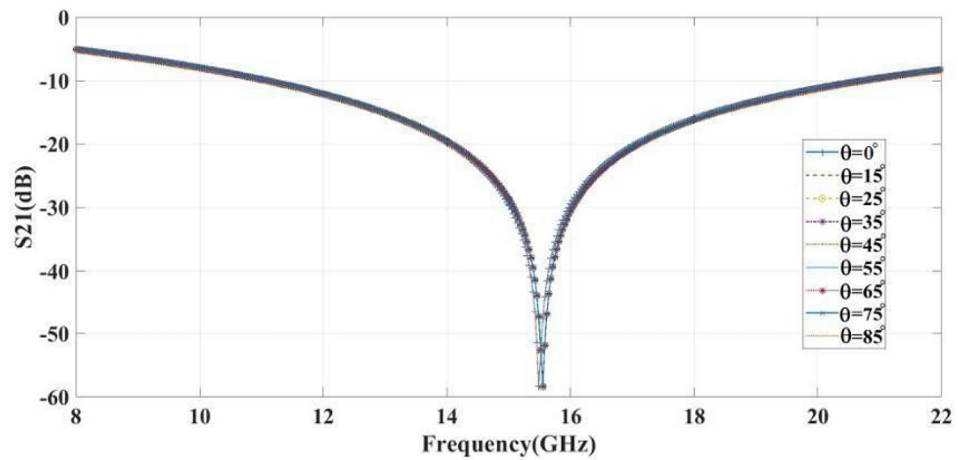
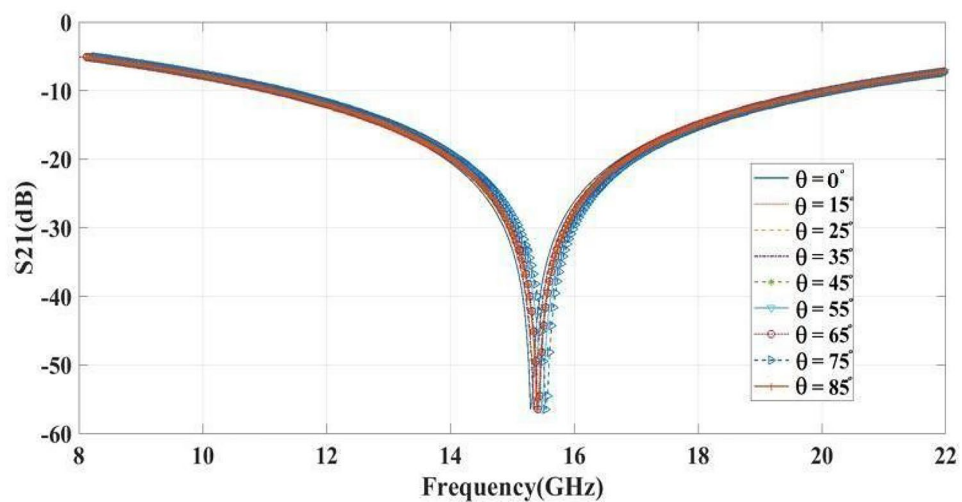


Fig. 15. Comparison results of combined loops with three-legged structure.



(a) TE Mode



(b) TM Mode

Fig. 16. Angular stability analysis of combined loops with three-legged structure.

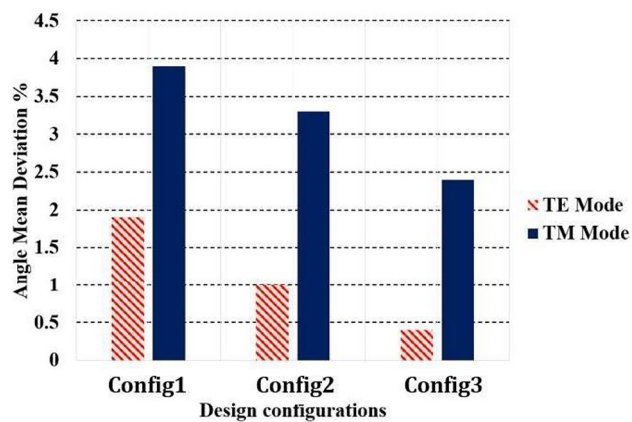


Fig. 17. AMD chart for different design configurations.

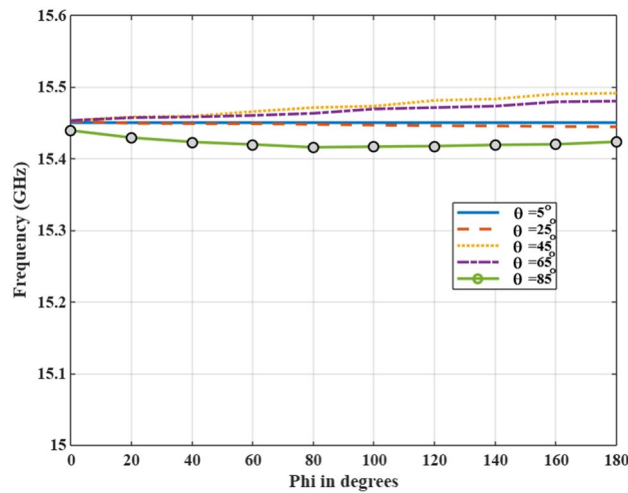


Fig. 18. Polarization analysis for various incident angle.

Phi/Theta angles	0°	5°	25°	45°	65°	85°	Mean
0°	0.00000	0.00000	0.00000	0.00000	0.00000	0.00000	0.00000
20°	0.00001	0.00040	0.00030	0.00050	0.00040	0.00120	0.000468
40°	0.00001	0.00010	0.00010	0.00010	0.00020	0.00020	0.000118
60°	0.00004	0.00020	0.00020	0.00030	0.00100	0.00100	0.000457
80°	0.00001	0.00001	0.00002	0.00040	0.00040	0.00020	0.000173
100°	0.00002	0.00020	0.00020	0.00020	0.00040	0.00100	0.000337
120°	0.00003	0.00003	0.00030	0.00030	0.00030	0.00020	0.000193
140°	0.00004	0.00040	0.00040	0.00040	0.00050	0.00030	0.00034
160°	0.00003	0.00030	0.00030	0.00050	0.00100	0.00100	0.000522
180°	0.00000	0.00001	0.00010	0.00010	0.00030	0.00020	0.000118
Frequency deviation	0.00001	0.00016	0.00019	0.00028	0.00045	0.00053	0.00027

Table 3. Frequency deviation (GHz) for various incident angles of polarization states.

can operate with a wide range of incident polarizations, providing greater flexibility and adaptability. To achieve polarization insensitivity, the surface must have a stable operating frequency for both polarized incident waves. Polarization insensitivity is often achieved by designing the metasurface with symmetric or isotropic meta-atoms (square loop, or cross-shaped structures). These shapes interact similarly with both transverse electric (TE) and transverse magnetic (TM) polarizations, ensuring that the metasurface response does not vary with polarization. We carefully choose unit cell dimensions and spacing, the metasurface can reduce phase dispersion, ensuring that the response remains stable across a wide range of incidence angles. This design minimizes signal degradation due to angle variations.

Figure 18 shows the S₂₁ curve for the configuration 3 (considered for angular stability) meta-atom with different polarizations, following a various incidence angle of 5° to 85°. At various angles, the unit cell has a stable operating frequency.

Further another key aspect is polarization insensitivity in metasurfaces, which refers to maintaining a consistent response regardless of the polarization state of incident signal. This is particularly important in practical applications where signal may be arbitrarily polarized. Usually, polarization insensitivity can be achieved by designing symmetric unit cells (e.g., circular or square geometries). This ensures that the metasurface responds similarly to both transverse electric (TE) and transverse magnetic (TM) polarizations. The resonating frequency for all the incident angles and theta values are approximately 15.48 GHz with minimum frequency deviation, which is tabulated in Table 3 from the data points of frequency deviation taken from Fig. 18.

The proposed system improves polarization insensitivity, with an average maximum deviation rate of approximately 0.027% for different polarized orientations. This demonstrates the system's stability and performance, making it a more versatile and efficient platform for manipulating electromagnetic waves.

Metasurface analysis

Surface which satisfies the metasurface properties possess several key characteristics that make them highly suitable for manipulating electromagnetic waves. The emergence of metasurface technology has opened up new opportunities in various applications by allowing for the precise manipulation of electromagnetic waves

in multiple dimensions. Furthermore, metasurfaces can be designed to exhibit unique phenomena that are not typically observed in conventional materials. For instance, metasurfaces can enable negative-angle refraction, where light is bent in a direction opposite to that predicted by Snell's law. Metasurfaces are often composed of subwavelength, periodically arranged unit cells, each with intricate geometries. Analysing each element individually across a large surface would be computationally intensive and impractical. EMT allows designers to approximate these unit cells collectively as a "homogenized" medium with effective material parameters (e.g., effective permittivity and permeability), which are averaged values or negative values that describe the behaviour of the entire metasurface. This simplification significantly reduces analysis complexity and computation time. And also, it helps to scaling up the array elements without changing its response. Due to their unique metasurface characteristics, an analysis of the effective medium theory is essential. However, in (8–10), the retrieval process for the effective medium parameters³⁴ is presented.

$$r \approx \frac{(1 - S_{21} + S_{11})}{jd(1 + S_{21} - S_{11})} \quad (8)$$

$$r = r + j \frac{S_{11}}{\lambda} \quad (9)$$

$$r = \sqrt{\frac{j d}{\lambda} \left\{ \frac{(S_{21} - 1)^2 - S_{11}^2}{(S_{21} + 1)^2 - S_{11}^2} \right\}} \quad (10)$$

Where d is the overall length of the loop structure, λ is the wavelength of the operating frequency.

Figure 19 illustrates the effective permeability (μ_r), permittivity (ϵ_r), and refractive index (η_r). In the effective medium, negative peaks occur at an operating frequency with substrate t and wavelength λ thickness. Figure 19 (a–c) displays that the permittivity, permeability, and refractive index curve deliver negative real and imaginary values at 15.1 GHz.

So, the design is a metasurface and confirms that the proposed system satisfies the left-handed behavior. metasurface properties. Additionally, modularity in the metasurface design allows for ease of scaling up or down depending on the specific application or coverage requirement, without changing the performances or properties of the metasurface shown in Fig. 20; Table 4.

• Results and discussions

The Metasurface prototype has been fabricated, as depicted in Fig. 21. The fabricated prototype has an overall dimension of 144 mm by 144 mm. It is made up of 32 by 32 elements separated at 0.24 mm. In future our approach with specific technique, like screen printing or photolithography, which is widely used in large-scale electronics manufacturing. These processes can produce metasurface in high volumes with precision at the Ku band frequency, making large-scale deployment more feasible. Further, the proposed design uses low-cost, flexible polymers with same properties of Rogers and metals as copper that are readily available and affordable, reducing material costs without compromising performance.

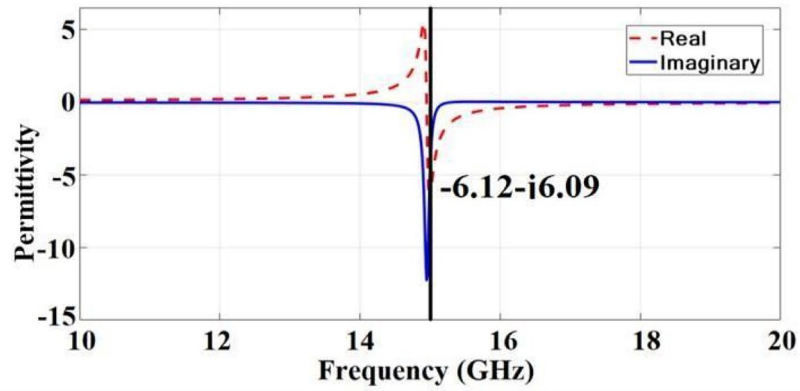
Real-world deployment requires resilience to factors like temperature fluctuations, humidity, UV exposure, and potential physical impacts. To address this, in future, this metasurface design will incorporate protective coatings, such as polymeric overlays or hydrophobic nanocoatings, which protect against environmental wear and corrosion. The durability testing indicates that the design withstands a wide range of temperatures and high humidity levels, making it suitable for both indoor and outdoor applications across diverse environments.

In setup Fig. 22, the constructed Metasurface is positioned in a fixture fitting with the absorbers surrounding it, and the two ridged horn antennas that are capable of functioning at frequencies ranging from 12 to 18 GHz are placed at the distance of 120 mm from the metasurface. One is used as transmitting antenna and another one is receiving antenna for the proposed metasurface structure. In this setup, the ridged horn antenna is placed at two adjacent sides of the fixed metasurface. Therefore, the appropriate outcomes are noted.

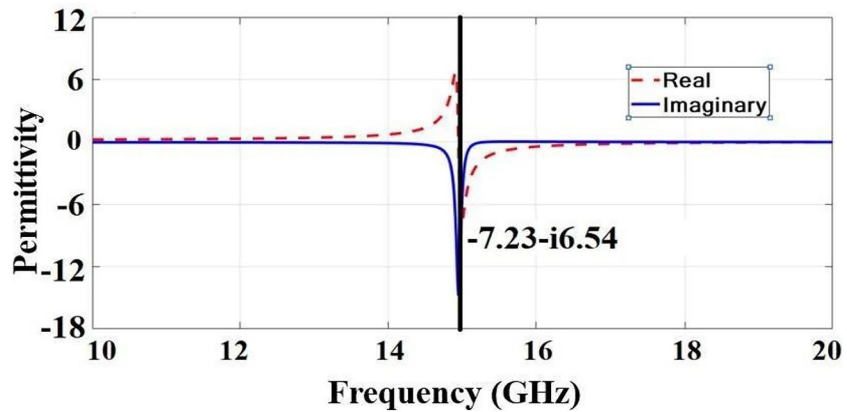
First, the transmission properties are measured without the metasurface using a movable handheld microwave analyser from Agilent Technologies (N9951A). Then, the transmission characteristics of the metasurface are recorded and obtained as reflecting characteristics at 12–18 GHz of band, and it can be shown in Fig. 23. The deviation observed between measured and simulated results might be due to minor variation in prototyping and the calibration settings. However, the reflecting performance at 15.5 GHz for the proposed structure is attained.

The evaluation of the validated results at various incident angles is shown in Fig. 24. The configuration 3 metasurface is observed to provide an angularly stability response for an EM wave up to 85°. The measurements produce TE and TM polarised results for measurement setup. In measured results, AMD% is about 0.45% for TE mode and 2.1% for TM mode. Therefore, the measured findings and the simulated results almost match. According to the measurement, the metasurface offers band-stop performance at 15.5 GHz with 60 dB of attenuation at 0°–85° of the incident waves. The measured results for TE polarisation and TM polarisation are good. Thus, the proposed metasurface exhibits polarisation independence due to its symmetrical design Table 5.

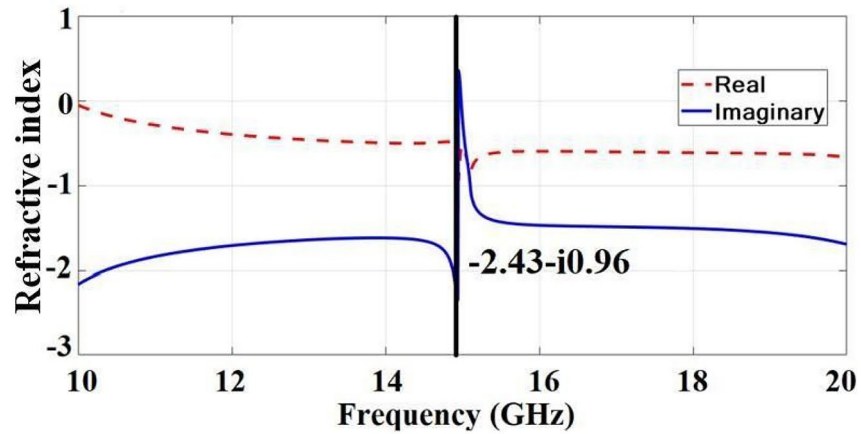
A comparative analysis is carried out to demonstrate further the effectiveness of the suggested metasurface with earlier designs. Table 5^{4,6–9} shows Operating frequency, structure characteristics, polarisation sensitivity, and angular stability comparisons. The proposed reflecting surface is a single-layer single-sided structure, so it allows compactness and scalability due to the increasing electrical length and meta-surface's features. Also, it provides a consistent response throughout a wide range of EM wave incident angles up to 85° with minimum frequency deviations, in contrast to the work^{4,6–9}, which provides limited angular stability with high frequency deviations. In addition, polarisation insensitivity is granted by the suggested metasurface due to the rotational



(a) Effective Permeability



(b) Effective Permittivity



(c) Refractive Index

Fig. 19. Metasurface analysis with effective medium.

symmetry of the tripole structure of the suggested metasurface. Thus, the proposed reflective frequency selective metasurface gives a wider bandwidth, superior angular stability, and polarisation insensitivity.

Conclusion

In this article, the electrical performance of the proposed metasurface structure for both TE and TM mode and different incidence angles of the EM wave have proposed, investigated, and experimentally validated. The proposed structure has employed in the operating frequency band of 12–18 GHz. The results show that the

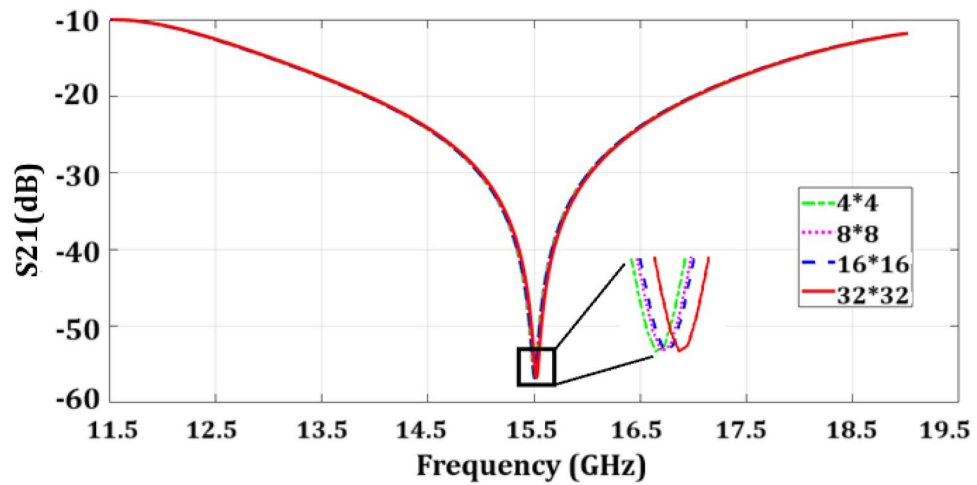


Fig. 20. Comparative analysis for various array structure.

S. No.	Array size	Operating frequency (GHz)	Frequency deviation (GHz)	
			Angle variation	Polarization variation
1	4*4	15.485	0.010	0.16
2	8*8	15.491	0.013	0.18
3	16*16	15.496	0.013	0.08
4	32*32	15.501	0.005	0.03

Table 4. Performances of various array structure.

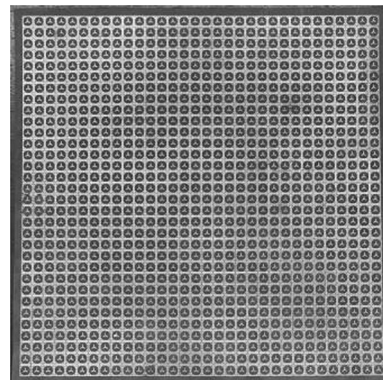


Fig. 21. Fabricated prototype of 32 × 32 proposed metasurface.

suggested structure has no impact on 32 × 32 elements, which result is the same as that of the unit cell. The suggested geometry for various incident angles, the shift in the operating frequency produced by TE and TM polarised waves is 0.45 and 2.1%, respectively, which is considerably small frequency deviations and provides a stable response in terms of the reflection parameters. The proposed metasurface structure offers significantly more angular and polarisation stability than the previous works. Further, the metasurface analysis supports the left-hand characteristics for downsizing the metasurface and controls the phase and amplitude of each element in the metasurface. So, the proposed structure will have more possibilities for using in RIS applications.



Fig. 22. Measurement setup with the proposed metasurface.

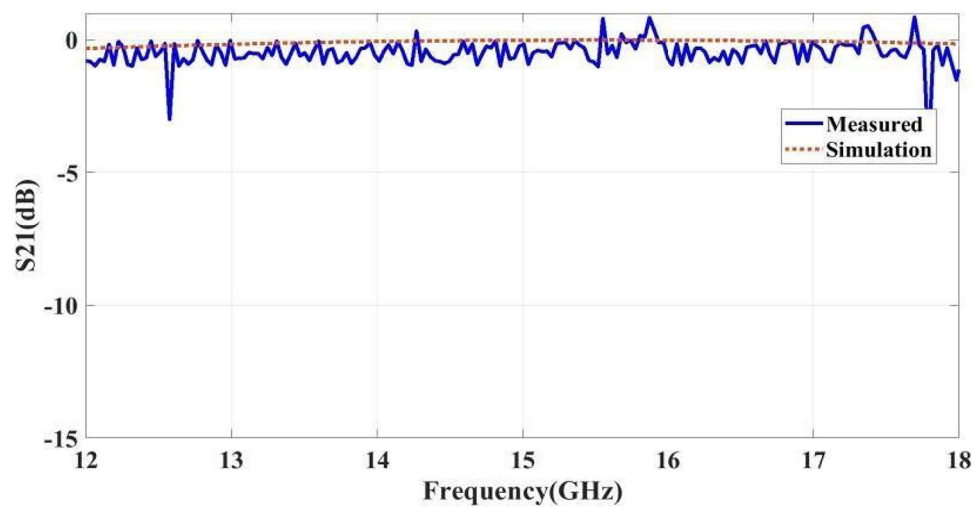


Fig. 23. Comparison results of transmission characteristics.

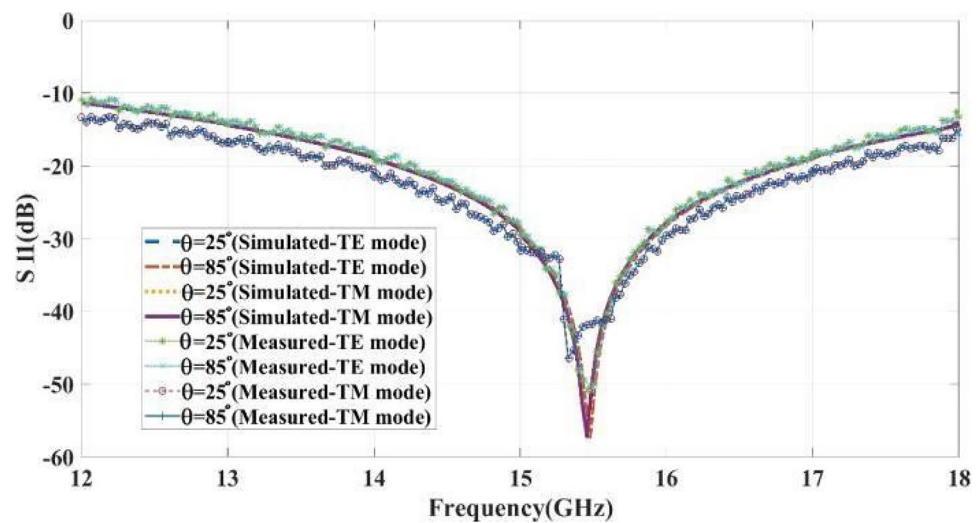


Fig. 24. Measure results of various incident angles at both modes of operations.

Ref.	Structure	Frequency (GHz)	Angular Stability	Frequency Deviation (GHz)		Polarization in- sensitivity
				TE Mode	TM Mode	
4	Symmetric	8–12	0°–80°	-	-	Yes
6	Symmetric	2.7	0°–60°	-	-	NA
7	Symmetric	5.8	0°–75°	0.07	0.92	Yes
8	Asymmetric	7.5	0°–60°	1.2	1.4	NA
9	Asymmetric	12.4,18,15.9	0°–60°	0.9	1.3	Yes
This work	Symmetric	15.5	0°–85°	0.02	0.19	Yes

Table 5. Comparison of research work 1 with recent works.

Data availability

The datasets used and/or analysed during the current study available from the corresponding author on reasonable request.

Received: 7 September 2024; Accepted: 24 December 2024

Published online: 02 January 2025

References

- Biglieri, E. et al. *H.: MIMO Wireless Communications-MIMO Wireless Communications* (www.cam-bridge.org, 2007).
- Wu, Q. et al. Intelligent Reflecting Surface Aided Wireless Communications: A Tutorial. (2020).
- Shao, X., You, C., Ma, W., Chen, X. & Zhang, R. Target sensing with Intelligent Reflecting Surface: Architecture and Performance. *IEEE J. Sel. Areas Commun.* **40** (7), 2070–2084 (2022).
- Chellaiah, E. An ultra-thin frequency-selective surface with inductive loading for X-band shielding applications. *Int. J. Commun. Syst.* **37**, 6: e5699 (2024).
- Krishnan, Rahul, R., Ganesan, K., Baskaran, A. G., Vimala, J. & Kalloor and A. SenthilKumar.: Survey on compact dual-Band stop frequency selective surface for shielding application. *Materials Today: Proceedings*, 47, 410–413, (2021).
- Mitra, R., Chan, C. H. & Cwik, T. Techniques for Analyzing Frequency Selective Surfaces—a Review. *Proceedings of the IEEE*, 76(12), 1593–161, (1988).
- Munk, B. A. Frequency Selective Surfaces. (2000).
- Xu, G., Hum, S. V. & Eleftheriades, G. A technique for Designing Multilayer Multi-stopband frequency selective surfaces. *IEEE Trans. Antennas Propag.* **66** (2), 780–789 (2018).
- Monorchio, A., Manara, G. & Lanuzza, L. Synthesis of artificial magnetic conductors by using multilayered frequency selective surfaces. *IEEE Antennas. Wirel. Propag. Lett.* **1**, 196–199 (2002).
- Liu, T. & Kim, S. S. Ultrawide Bandwidth Electromagnetic Wave absorbers using a high-capacitive folded spiral frequency selective surface in a Multilayer structure. *Sci. Rep.* **2019**, **9** (1), 1–10 (2019).
- Wu, B. et al. Design and validation of flexible multilayer frequency selective surface with transmission Zeros. *IEEE Antennas Wirel. Propag. Lett.* **18** (2), 250–254 (2019).
- Rashid, A. K., Li, B. & Shen, Z. An overview of three-dimensional frequency-selective structures. *IEEE Antennas Propag. Mag.* **56** (3), 43–67 (2014).
- Luo, X. et al. Cascaded metasurface for simultaneous control of transmission and reflection. *Opt. Express.* **27** (Issue 6), 9061–9070 (2019).
- Wang, Q. et al. Optically reconfigurable metasurfaces and photonic devices based on phase change materials. *Nat. Photonics.* **10** (1), 60–65. <https://doi.org/10.1038/nphoton.2015.247> (2016).
- Genevet, P., Capasso, F., Aieta, F., Khorasaninejad, M. & Devlin, R. Recent advances in planar optics: from plasmonic to dielectric metasurfaces. *Optica* **4** (1), 139–152. <https://doi.org/10.1364/OPTICA.4.000139> (2017).
- Shalaginov, M. Y., An, S. & Zhigang, Y. Reconfigurable all-dielectric metalenses with diffraction-limited performance. *ACS Nano.* **13** (3), 3455–3466. <https://doi.org/10.1021/acsnano.9b00170> (2019).
- Chen, H. T., Taylor, A. J. & Yu, N. A review of metasurfaces: physics and applications. *Rep. Prog. Phys.* **79** (7), 076401. <https://doi.org/10.1088/0034-4885/79/7/076401> (2016).
- Tsai, W. Y., Chu, C. H. & Tsai, D. P. Progress in multi-functional metasurfaces for optical imaging and sensing. *J. Phys. D.* **52** (48), 483001. <https://doi.org/10.1088/1361-6463/ab3d56> (2019).
- Kamali, S. M., Arbabi, E., Arbabi, A. & Faraon, A. A review of dielectric optical metasurfaces for wavefront control. *Nanophotonics* **7** (6), 1041–1068. <https://doi.org/10.1515/nanoph-2017-0120> (2018).
- Smith, J., Johnson, A. & Kumar, M. Metasurface applications in 5G and beyond. *IEEE Trans. Commun.* **69** (5), 1010–1023 (2022).
- Zhang, L., Wang, H. & Chen, Y. Multi-layer metasurfaces for enhanced bandwidth and beamforming. *IEEE Trans. Antennas Propag.* **68** (12), 2087–2098 (2021).
- Lee, J. & Park, S. Frequency-selective multi-layer metasurfaces for interference management. *J. Appl. Phys.* **129**, 102–111 (2021).
- Wu, Y., Liu, X. & Zheng, Q. Graphene-based tunable metasurfaces for terahertz applications. *Appl. Phys. Lett.* **112** (8), 081101 (2020).
- Tan, S. & Zhao, L. Liquid crystal-based reconfigurable metasurfaces for millimeter-wave communications. *Opt. Express.* **28** (10), 13445–13456 (2020).
- Wang, T., Li, R. & Feng, D. Intelligent reflecting surfaces for beyond-5G networks: design and optimization. *IEEE Commun. Mag.* **58** (7), 102–108 (2020).
- Kim, H. & Choi, J. Reconfigurable holography for high-density networks. *Nano Commun. Netw.* **22**, 38–48 (2021).

27. Li, Y., Xu, J. & Zhao, P. MEMS-integrated multi-layer metasurfaces for dynamic phase control. *IEEE Photon Technol. Lett.* **33** (4), 532–535 (2021).
28. Chen, M. & Verma, A. AI-enabled optimization of reconfigurable metasurfaces. *IEEE Internet Things J.* **7** (6), 5142–5150 (2020).
29. Zhang, F. & Lin, L. Thermal management in high-frequency metasurfaces. *IEEE Trans. Microw. Theory Tech.* **67** (9), 3903–3910 (2021).
30. Huang, X. & Zhao, Z. Scalable manufacturing techniques for multi-layer metasurfaces. *Adv. Mater.* **32** (18), 187014 (2022).
31. Anwar, R. S., Mao, L. & Ning, H. Frequency Selective Surfaces: A Review. *Applied Sci-ences Vol. 8*, Page 1689, 8(9), 1689, (2018).
32. Ferreira, D., Caldeirinha, R. F. S., Cuinas, I. & Fernandes, T. R. Square Loop and slot frequency selective surfaces Study for Equivalent Circuit Model Optimization. *IEEE Trans. Antennas Propag.* **63** (9), 3947–3955 (2015).
33. Selvaraj, M., Vijay, R., Anbazhagan, R. & Rengarajan, A. Reconfigurable metasurface: enabling tunable reflection in 6G wireless communications. *Sensors* **23** (22), 9166 (2023).
34. Faruque, M. R. I., Hasan, M. M. & Islam, M. T. Tree-shaped fractal meta-surface with left-handed characteristics for absorption application. *Appl. Phys. A: Mater. Sci. Process.* **124** (2), 1–8 (2018).

Author contributions

Ramya Vijay wrote the main manuscript, Monisha Selvaraj worked on the preliminary design and analysis; Rajesh Anbazhagan involved in prototyping and measurement.

Declarations

Competing interests

The authors declare no competing interests.

Additional information

Supplementary Information The online version contains supplementary material available at <https://doi.org/10.1038/s41598-024-84523-9>.

Correspondence and requests for materials should be addressed to R.V.

Reprints and permissions information is available at www.nature.com/reprints.

Publisher's note Springer Nature remains neutral with regard to jurisdictional claims in published maps and institutional affiliations.

Open Access This article is licensed under a Creative Commons Attribution-NonCommercial-NoDerivatives 4.0 International License, which permits any non-commercial use, sharing, distribution and reproduction in any medium or format, as long as you give appropriate credit to the original author(s) and the source, provide a link to the Creative Commons licence, and indicate if you modified the licensed material. You do not have permission under this licence to share adapted material derived from this article or parts of it. The images or other third party material in this article are included in the article's Creative Commons licence, unless indicated otherwise in a credit line to the material. If material is not included in the article's Creative Commons licence and your intended use is not permitted by statutory regulation or exceeds the permitted use, you will need to obtain permission directly from the copyright holder. To view a copy of this licence, visit <http://creativecommons.org/licenses/by-nc-nd/4.0/>.

© The Author(s) 2024